# Spatially Resolving Lithium-Ion Battery Aging by Open-Hardware Scanning Acoustic Imaging

David Wasylowski<sup>a,c,\*</sup>, Niklas Kisseler<sup>a</sup>, Heinrich Ditler<sup>a,c</sup>, Morian Sonnet<sup>a,c</sup>, Georg Fuchs<sup>a,e</sup>, Florian Ringbeck<sup>a,c</sup>, Dirk Uwe Sauer<sup>a,b,c,d</sup>

<sup>a</sup> Chair for Electrochemical Energy Conversion and Storage Systems, Institute for Power Electronics and Electrical Drives (ISEA), RWTH Aachen University, Jägerstrasse 17-19, 52066 Aachen. Germany

<sup>b</sup>Institute for Power Generation and Storage Systems (PGS), E.ON ERC, RWTH Aachen University, Mathieustrasse 10, 52074 Aachen, Germany

<sup>c</sup> Jülich Aachen Research Alliance, JARA-Energy, Templergraben 55, 52056 Aachen, Germany

<sup>d</sup>Helmholtz Institute Münster (HI MS), IEK 12, Forschungszentrum Jülich, 52425 Jülich, Germany

<sup>e</sup>Safion GmbH, Hüttenstraße 7, 52068 Aachen, Germany

# Abstract

The internal mechanical condition of a lithium-ion battery is often disregarded but delivers essential information about the battery performance and lifetime. This work presents a method to measure the internal mechanical condition of lithium-ion cells with high spatial resolution through scanning acoustic imaging. An open-hardware ultrasound scan set-up has been engineered to increase the availability of acoustic imaging significantly. Using this set-up, three cells that were aged and clamped at different pressures have been imaged. The resulting ultrasound image clearly showed which parts of the cells have more severely aged than others. The cells which were clamped with the highest examined pressure (5 and 10 bar) showed the strongest covering layer and gas formation in the ultrasound scan. The mechanical effect of the aging seen in the ultrasound image was verified for each cell by conventional electrical and post-mortem analysis. At locations where the ultrasound image showed distinct irregularities, scanning electron microscopy images identified mossy surface layers typical for lithium

<sup>\*</sup>Corresponding author, Tel.: +49 241 80 49390, Fax: +49 241 80 92203 Email address: david.wasylowski@isea.rwth-aachen.de (David Wasylowski) URL: www.isea.rwth-aachen.de (David Wasylowski)

plating.

Keywords:

ultrasound, lithium plating, scanning acoustic microscopy, non-destructive testing

# 1. Introduction

The permanent demand for emission reduction and oil independence results in an electrification process, which predominantly takes place in the automotive sector [1]. Lithium-ion (Li-ion) batteries are, due to their exceptional combination of high energy and power density, the current choice for energy storage in most electric vehicles [2]. Unfortunately, Li-ion batteries' usage also poses additional risks, mainly due to their emission of hazardous compounds and rapid heat release in the case of thermal runaway [3]. The actual risk was painfully demonstrated by, e.g., Boeing, leading to the temporary grounding of all Boeing 787 Dreamliners and tremendous financial losses [4]. As a result, there exists an urgent need for intelligent supervision systems, which, non-destructively, probe the battery's internal condition and sense if all relevant operating conditions are not detrimental to the battery regarding safety and lifetime. Especially the information about the internal mechanical condition of the battery is crucial, as it holds valuable information about the electrochemical performance and vice versa [5]. Consequently, a full-scale non-destructive test (NDT) of the cell would be beneficial during all phases of its life cycle to gather information for further development.

There are several possibilities to perform NDT on Li-ion cells such as computed tomography (CT), magnetic resonance imaging (MRI), pulse thermography and neutron-based characterization methods, each with its advantages and disadvantages [6, 7, 8]. The main disadvantage that these methods have in common is that they require either a lot of space, time or financial resources. First reported by Hsieh et al. [9] and later reproduced and modified by many others, is the NDT application of ultrasound (US) through-transmission on Li-ion cells,

which has promising properties to overcome the above disadvantages. This method uses the electrical stimulation of piezoceramics (or the sensors made of them) to generate ultrasonic waves in the frequency range from 200 kHz to tenths of MHz. In most publications, bulk waves are stimulated. These waves are characterized by the fact that they only have either a transverse or a longitudinal component.

When an ultrasonic wave with the amplitude  $A_i$  located in a medium with a mechanical impedance  $Z_1$  strikes a material interface to a medium with a mechanical impeadance  $Z_2$  at normal incidence, it is partially reflected and transmitted. The reflected  $(A_r)$  and transmitted  $(A_t)$  wave amplitudes are described by the following equations.

$$A_r = \left(\frac{Z_2 - Z_1}{Z_1 + Z_2}\right) A_i \tag{1}$$

$$A_t = \left(\frac{2Z_2}{Z_1 + Z_2}\right) A_i,\tag{2}$$

with

$$Z_i = \rho_i \left( K_i + \frac{4}{3} G_i \right) \quad \text{with } i = 1, 2.$$
 (3)

Here  $K_i$  and  $G_i$  are the compression and shear modulus, respectively, which can be calculated from the modulus of elasticity E using Poisson's ratio, and  $\rho_i$  the density. This results in the fact that at the interface of media with similar mechanical impedances there is little to no reflection and mostly transmission and vice versa for very differing impedances [10].

Numerous publications have proven that the measured US signal is influenced by the cell's state of charge (SoC) and health (SoH). The ultrasonic waves SoC sensitivity is caused by the fact that during cycling of a cell, the elastic modulus and density of the active material is changing due to electrochemical and structural changes from intercalation and deintercalation of lithium-ions [11]. The ultrasonic waves SoH sensitivity is caused by material changes during aging, such as particle cracking, the formation of gaseous products, the growth of a solid electrolyte interface (SEI), or other covering layers [12, 13, 14, 15]. Espe-

cially because those aging phenomena have a very strong influence on the elastic modulus and density, ultrasound technology is well suited for aging diagnostics [16]. Both the SoC and SoH diagnostic capabilities have been demonstrated many times in recent years. In [17] a support vector regression machine learning model has been trained to improve the SoC prediction of LCO cells over several hundred cycles using the time of flight (ToF) and signal amplitude (SA) of a measured ultrasound signal. An SoC prediction of up to 1% has been achieved.

Building on the previous publications, Wu et al. specifically investigated the increased aging, or abuse of the cell in their work [18]. This work demonstrated the usefulness of ultrasound in SoH estimation and showed how sensitive ultrasound is in detecting gases in a battery cell. Both the ToF and the SA immediately showed distinct irregularities when introducing gas particles into the cell caused by overcharging.

All of the publications mentioned above are limited by the fact that they just measured the ultrasound in few discrete locations on the cell surface. Since cell aging is very inhomogeneous, it is never clear with setups with fixed sensors to what extent the aging is adequately measured [19]. Therefore, it would be desirable to build a structure where the position of the sensors is variable so that the entire cell can be measured. This method is also known as scanning acoustic microscopy (SAM) or scanning acoustic imaging. In a very recent study by Bauermann et al., a commercial SAM microscope was used to localize defects in an LCO Li-ion cell for the first time [20]. Unfortunately, the high cost of such an SAM microscope impedes market and research penetration. In addition, due to the used sensors, the entire cell cross-section could not be measured. In the following, a cost-effective set-up is presented with which the entire cell cross-section can be measured simultaneously. This framework is going to be used to localize aging phenomena of three identical pouch cells aged at different clamping pressures. The focus of this work is to present a tool and its possibilities for future publications. To accomplish this, all relevant underlying effects that occur during the experiments are analyzed to demonstrate the diagnostic capabilities of the framework.

## 2. Experimental Set-Up and Methodology

There are generally two ways to measure ultrasound propagation: the pitch-catch (also called through-transmission) method and the pulse-echo method. With the pitch-catch method, at least two ultrasound transducers are used. One always serves as the transmitter and the other as the receiver. Usually, the two transducers are placed opposite each other, with the battery cell in the middle. With the pulse-echo method, only one transducer is used, which simultaneously serves as transmitter and receiver. Here the reflection of the emitted ultrasonic wave is measured according to equation (1) to (3) [10].

The experiments were carried out with a self-developed SAM imaging device, which was specially designed for ultrasound measurements on pouch cells of variable size. The device consists of two independently operable measuring arms, each of which can automatically move the corresponding ultrasonic transducer in all three spatial directions. This allows measurements to be made using both the pulse-echo method and the through-transmission method on a normal or diagonal measurement path.

# 2.1. Design and Features of the Custom SAM Microscope

To achieve a sufficient positioning accuracy to generate an adequate image at comparatively low costs, a system of stepper motors, trapezoidal thread spindles and precision linear guides was engineered (see figure 1). The NEMA-14 stepper motors are operated using commercially available stepper motor drivers and microcontroller boards. The detailed documentation of the structure is provided open-hardware in our git repository to expand the availability of SAM measurements [21]. The maximum achievable resolution (in other words, lowest length/pixel) of the measurement is 5  $\mu$ m/pixel. This can be either increased or decreased by changing the focal beam diameter of the sensor or using higher precision motors. In the context of this work, a coarser resolution of 500  $\mu$ m/pixel

and 2000  $\mu$ m/pixel was chosen. On the one hand, this reduces the scan time quadratically, and, on the other hand, it is not clear with the self-built sensors how large the beam's diameter is. This would require further simulations, which shall not be part of this work. However, as will be shown, the apparatus can generate adequate images even with the coarsest resolution chosen here.

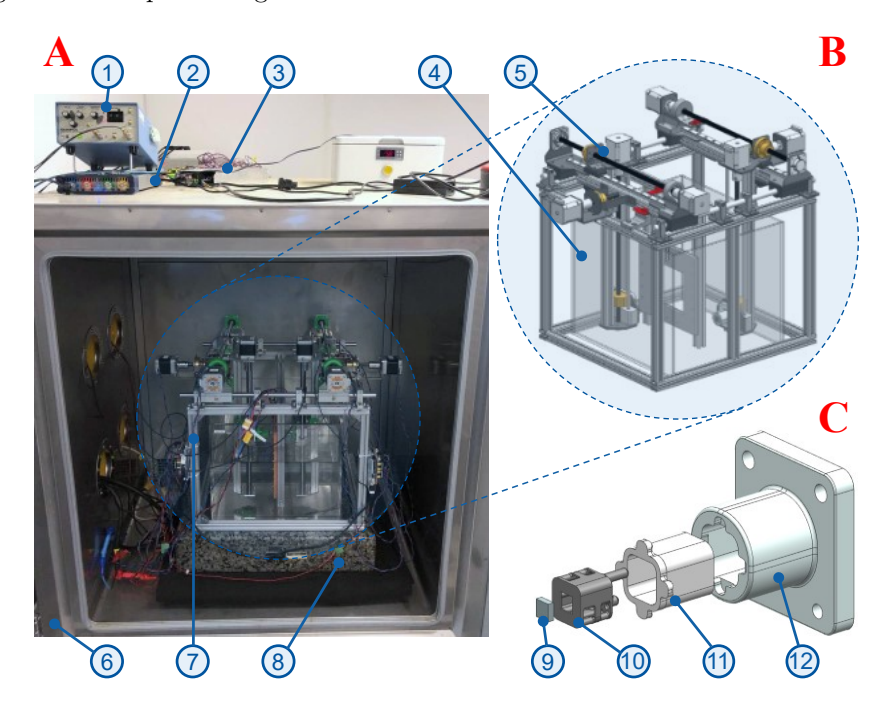


Figure 1: **A**: Picture of the developed SAM set-up. Consisting of the ultrasonic pulser/receiver (1), USB oscilloscope (2), 12 V power supply for the stepper motors (3), climate chamber (6), SAM set-up (7) and granite foundation plate (8). **B**: CAD rendering of the SAM set-up consisting of trapezoidal thread spindles, stepper motors and precision linear guides (5) and a silicone oil tank (4). **C**: Exploded-view drawing of the custom-made ultrasonic transducers, consisting of the piezoceramic (9), 3D-printed parts for the stabilization of the piezoceramic connection (10), housing for the filling material (11) and for mechanical connection to the measurement arm (12).

The US measurements were carried out using the through-transmission method. Meaning the ultrasound wave is stimulated on one side of the cell and received on the opposite side. For this purpose, the measuring system was equipped with two ultrasonic transducers. To further decrease the total system cost, the transducers were also self-build. Both transducers have a centre frequency of 1 MHz. The core element of each transducer is a piezoceramic made of modified lead zirconate titanate of the type PIC255 from the manufacturer PI Ceramic GmbH with external dimensions of 10.0 mm x 10.0 mm x 2.0 mm (LxWxH). The piezoceramics are clamped in an additively manufactured housing and cast in with a two-component epoxy resin. The model 5077PR from the manufacturer Olympus NDT is used as the pulse generator/pulse receiver. The received signal is sampled at 125 Msps with a USB oscilloscope of the type 6404D (PicoScope) from the manufacturer Pico Technology. These two or similar devices should be already available in most laboratories of ultrasound research groups so that this set-up offers a low entry barrier from classical one-dimensional ultrasound research into SAM imaging

The examined pouch-bag battery cell was positioned upright in a container filled with silicone oil and fixed at the circumferential sealing seams via a plastic frame. The cell tabs are not in contact with the silicone oil, which serves as a coupling medium. Due to its low electrical conductivity, the silicone oil prevents the battery cell from discharging unintentionally if it contacts the cell tabs accidentally, even if externally introduced particles contaminate it. The kinematic viscosity of the silicone oil used is 20 cSt, which is comparable to water. All measurements were carried out at a constant ambient temperature of 25 °C. For this purpose, the entire measuring apparatus was positioned in a climate chamber (model XB-OTS-408 by Dongguan Xinbao Instrument Co., LTD). The measurement setup was placed on a granite foundation plate to dampen any vibrations from the climate chamber.

# 2.2. Examined Cell and Preceding Aging Tests

For the measurements, the Li-ion cell of the manufacturer Kokam of the type SLPB526495 with a capacity of 3.3 Ah and an external dimension of 95.0 mm x 64.0 mm x 5.4 mm (LxWxH) was used. The stack design of the cell consists of two individually Z-folded units connected in parallel. Each unit contains six double side coated graphit anodes, five double side coated Li(NiCo)O<sub>2</sub> cathodes

Table 1: List of examined cells including correspondig clamping, cycling conditions and last measured residual capacity at end of life (EoL) including the corresponding full cycle count.

cell ID	clamping	cycling	capacity & cycles @ EoL
cell 1	constant-path 0.5 bar	1C, 100 % DOD	$91~\%$ @ $580~\mathrm{cycles}$
cell 2	constant-force 5 bar $$	1C, 100 % DOD	$75.5~\%$ @ $420~\mathrm{cycles}$
cell 3	constant-force 10 bar	1C, 100 % DOD	$76.8~\%$ @ $160~\mathrm{cycles}$

and two single side coated cathodes with the second stack containing an additional double side coated cathode [22]. The examined cells were clamped using two different clamping methods: constant-path and constant-force clamping. The resulting aging protocol with the corresponding cells can be found in table 1. For constant-force clamping two aluminium pressure plates were subjected to a constant-force applied by four compression springs corresponding to an equivalent surface pressure of 5 bar (cell 2) or 10 bar (cell 3) (see figure 2B). For the constant-path clamping, the aluminium plates are fixed to the cell with nuts and bolts (see figure 2C). The initially applied pressure was 0.5 bar (cell 1). The bolts are held in place by wedge lock washers on both sides of the two outer aluminium plates to prevent the nuts from loosening due to vibration in the test environment. The applied compressive forces for both set-ups were measured by means of a load cell (KM38 by ME-Meßsysteme GmbH) using a third aluminum plate. In addition, steel plates were fixed between the cell and the aluminium plate. These steel plates had cutouts that made the bracing slightly inhomogeneous. However, as will be shown, other aging effects are much more significant, so the influence of this slight inhomogeneity can be neglected. The cells were then cycled under constant current constant voltage (CC CV) conditions at a charge rate of 1C with a depth of discharge (DOD) of 100 % until they reached a residual capacity of less than 80 % during a check-up except for cell 1. The trajectory of the residual capacity of the cells is shown in figure 2. The capacities shown here have all always been measured in the clamped state. After completion of the aging tests, the cell was stored unclamped at constant room temperature of 25 °C for a further 9 months until the SAM measurements. The focus of this work is not on describing and analysing the aging mechanisms at different pressures and clamping methods but rather on the spatially resolved ultrasonic imaging of those. Nevertheless, the effects of the different pressures and clamping methods and their visibility in the ultrasound image are described and corroborated with the literature in the following.

## 2.3. Influence of External Pressure on Cell Aging

The accelerated aging of Li-ion cells under increased mechanical stress is the subject of current research at various research institutions. In [23] Cannarella et al. conducted very similar clamping experiments with three commercial LCO pouch cells clamped at 0.5, 5, and 50 bar. As a function of the cycle number, the normalized capacity evolution showed higher capacity fade at higher clamping pressures. According to the results in [23], the main reason for the capacity fade is loss of lithium inventory (LLI), since a post mortem analysis showed that the half cells have higher capacities than the corresponding full cells. At higher pressures, according to [23] inhomogeneities from the production process are amplified, which leads to increased local clogging and deformation of the separator and thus to more covering layer formation due to local current density increases. An additional effect studied in [24] is the decrease of available active surface area at higher clamping pressures due to mechanical compression of the active materials' particles. According to the study, this additionally might lead to increased current density and ultimately kinetic retardation that enhances side reactions. Since the examined cells and measurement setups in [23] and [24] are very similar to the ones used in this work, we can assume that the aging results will have a similar trend and similarly caused side reactions.

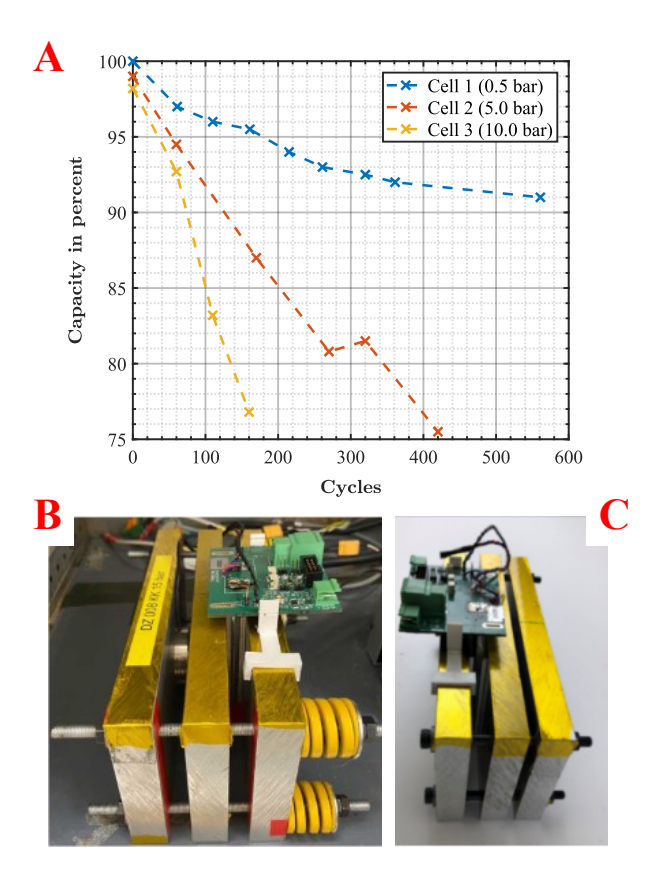


Figure 2: A: Trajectory of the 1C residual capacity during the check-ups of the examined cells. The accelerated aging at higher pressures is clearly visible. The crosses indicate the time of check-up. All capacities shown here are measured in the clamped state. B: Picture of the constant-force clamping set-up. C: Picture of the constant-path clamping set-up.

# 3. Results and Discussion

The cycling of the clamped cells results in three very differently aged cells. In figure 2A it can be seen that the aging curve of cell 1 is significantly flatter than that of the cells cell 2 and cell 3. Furthermore, capacity difference analyses (CDA) showed that the aging effects in the high pressure cells are different from those in the low pressure cell [25]. According to Lewerenz et. al., this could be due to an increased formation of a covering layer. The results are consistent with the investigations from the literature (see chapter 2.3). Figure 3 shows

photos of the front and back of the cells examined under pressure before they were scanned in the custom made SAM imaging device. The markers indicate

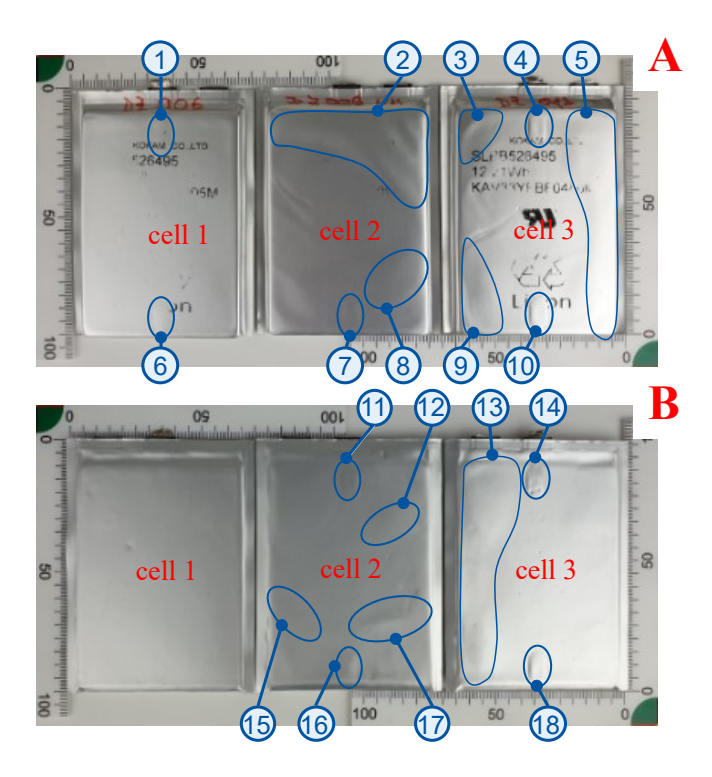


Figure 3: **A**: Picture of the front side of the cells aged under pressure. **B**: Picture of the back side of the cells examined under pressure. Reading from left to right, first cell 1, then cell 2 and lastly cell 3 is shown. The most noticable bulges are marked. Through optical inspection it is apparent that the cell cycled with the lowest pressure has fewer bulges.

clear bulges in the cell housing. It should also be noted that the cells have been turned vertically to the back (in figure 3B) and the left side of the cell back is in the same position as the right side of the cell front. These bulges most likely indicate gas or covering layer accumulation even before the SAM analysis. However, it is not clear in advance exactly what the overall extent of degradation is or if there are gas accumulations within the cell stack. cell 1 shows significantly fewer bulges. The smaller oval columns on the top and bottom of

the cell (marker 1 and 6) are rather to be understood as non-stressed areas and originate from the cut-outs in the steel plates. Although it may appear that this has made the clamping highly inhomogeneous, it will be shown later that this effect is negligible compared to the strong degree of clamping.

#### 3.1. SAM Analysis

After optical inspection of the cell housing, the three previously clamped cells were placed in the custom SAM microscope. To demonstrate both high resolutions and scan times, between which a trade-off has to be made, cell 3 was scanned with a spatial resolution of 500 µm/pixel and cells cell 2 and cell 1 with a spatial resolution of 2000 μm/pixel. When a new scanning position is reached, the system waits one eighth of a second to allow any possible swirling of the silicone oil to settle. However, this safety margin is most probably much larger than necessary, as no swirling was observed in this set-up for such small steps. Significantly shorter scan times can be achieved by reducing the safety margin or even omitting it altogether. However, this has not vet been done at this stage of development. The resulting scan times for  $7000 \, mm^2$  are 12 min for  $2000 \mu m/pixel$  spatial resolution and 45 min for 500  $\mu m/pixel$  spatial resolution. Even at this stage of development, these are remarkable improvements compared to classical imaging techniques listed in chapter 1. Of course, significantly higher resolutions can be achieved with the methods from chapter 1, but the focus of the apparatus developed in this work is rather on an optimal cost-use-time ratio.

## 3.1.1. Data Processing and Feature Extraction

At each measuring point, an ultrasonic signal is recorded with the sampling rate of 125 Msps for 10000 samples. The signal is a linear combination of incoming ultrasound wave modes, noise as well as other signal components. The so-called continuous wavelet transform (CWT) is used to design a bandpass filter, subsequently applied to the raw signal. The CWT is a convolution (see equation 4) that shows which signal components of the signal f(t) have a high similarity to the so-called mother wavelet  $\psi(t)$ , at different scales (a)

and translations (b) [26]. These components appear brighter in the CWT than components with low similarity (see figure 4).

$$C(a,b) = \frac{1}{a} \int_{-\infty}^{\infty} f(t)\psi^* \left(\frac{t-b}{a}\right) dt$$
 (4)

The choice of the mother wavelet is essential to reach a good trade-off between spectral and temporal resolution. Preliminary analysis has shown that the morlet mother wavelet allows for good separation of the different oscillation modes present here while keeping a good temporal resolution. Hence it is used in all following experiments for analysis. The big benefit of the CWT in this application is that it can distinguish the difference between the longitudinal mode of interest (centre frequency 1 MHz) and the low frequency transversal mode (center frequency 150 kHz) much clearer than fast fourier transform methods [27]. The superimposed low frequency transversal mode has a different speed of sound and attenuation, changing the time of flight (ToF) and other important ultrasound features and therefore needs to be filtered out (see zoom in figure 4). The resulting CWT can be seen in Figure 4. It is obvious that most of the signal has frequency components in the range 50 kHz to about 2 Mhz. Thus, the bandpass filter is designed according to the bandwidth of the longitudinal signal in the CWT (500 kHz to 3 Mhz). There is some electromagnetic interference (EMI) ringing visible in the beginning of the shown signal which has a much higher frequency and is also filtered out. The result is depicted as the red filtered signal in figure 4. All control and signal processing code was written in Python as this is allowing for easy communication with both the microcontrollers and the USB oscilloscope while using the robust signal processing frameworks. Based on the filtered signal, the entire spectrum of imaging techniques is at hand. In the context of this work, two imaging methods are presented in comparison. In a first approach, the maximum amplitude (SA) of the signal is used and a colour is assigned to it linearly. The resulting image can be seen in figure 5 in the first column. In [20], the one-dimensional feature of the weighted ToF of reflected ultrasonic waves was used as the imaging method. However, in order to go one step further in the imaging procedure in this work, the so-called signal intensity

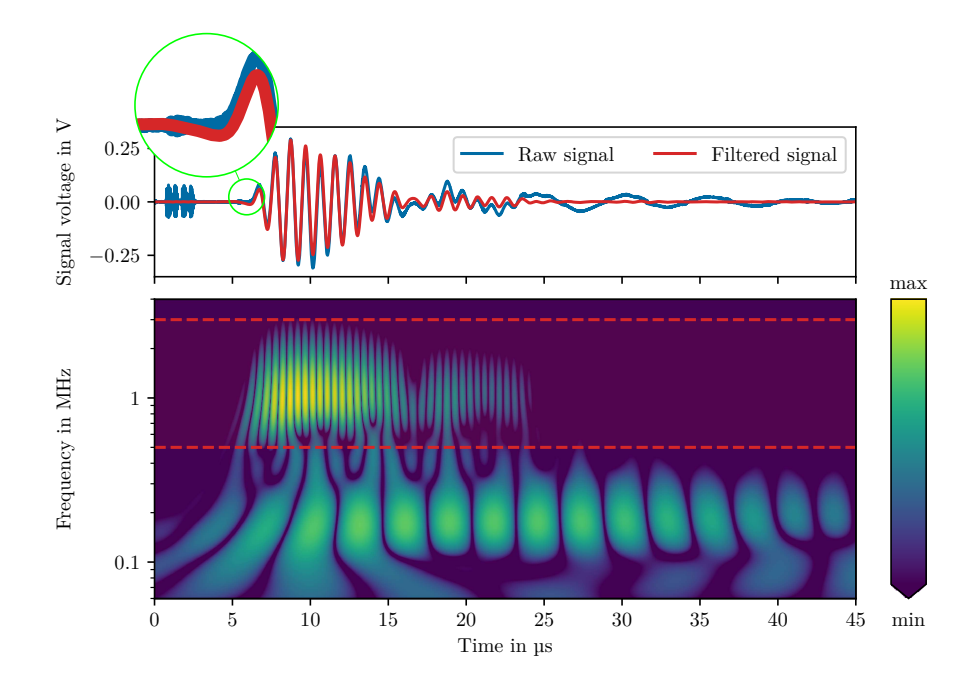


Figure 4: Continuous wavelet transformation (CWT) of a exemplary raw ultrasonic signal and comparison with the filtered signal. The filtering of the wavemode of interest is clearly visible. The red lines in the CWT amplitude indicate the width of the subsequently applied bandpass filter.

(SI) is used [10]. The SI is defined as an integral over all squared signal samples of the filtered signal  $f_{filt}(t)$  during the measurement time  $t_N$ .

$$SI = \int_0^{t_N} f_{filt}^2(t) dt \tag{5}$$

This makes it possible to take into account information that does not only show up in one or a few samples. The resulting images are shown in figure 5 in the second column. There are many other methods to interpret the ultrasound data into an image for example using time-frequency analysis. However, these are beyond the scope of this paper and are subject of further research.

## 3.1.2. Discussion of SAM Images

On the basis of the signal processing methods presented in previous sections, the most relevant spots in the SAM images depicted in figure 5 are now discussed.

Cell 2 (in figure 5B) has undergone both the most severe electrical aging (see figure 2A) and shows the most severe inhomogeneities in the SAM images. These inhomogeneities occur, amongst others, at the places where in figure 3 bulges can be optically inspected. However, there are almost as many spots (such as the middle ellipse in figure  $5\mathbf{B}$ ) where no bulges are visible, but where an inhomogeneity is visible in the SAM image. Based on equations 1–3, the spots with a weak signal amplitude (blue spots in the first column) are caused by a significantly different mechanical impedance in the signal path. The current understanding according to [28] and [20] is that this difference in impedance is due to inhomogeneous electrolyte distribution, gas accumulation or other covering layers. In recent studies, it was not possible to distinguish which particular effect is responsible for which change in the SAM image. However, since according to Deng et. al. gases have a very different mechanical impedance compared to active material, the blue spots in the signal amplitude plot can be attributed to an increased gas accumulation. Furthermore, it can be suspected that especially round or elliptical spots in the SAM image reflect gas bubbles, as these shapes represent energetically favourable states for gases. This indication is confirmed by the fact that no covering layers or electrolyte accumulations were visible on the anode sheet at these elliptical spots. It is also worth noting that the through-transmission method resulted in a complete scan of every cell layer at every point and thus also found gas accumulations that were located in the middle or even on the back of the cell. For example, the gas accumulations located in circle 17 in figure 3B are visible in the signal amplitude image 5B, although they were located on the back side of the cell, as well as various other inhomogenities located in the marked ellipses that cannot be assigned to either the front or the back side of the cell and were thus presumably located in the middle of the cell stack. The trade-off of the through-transmission method is that although the entire cell cross-section can be measured very quickly with the same sensor, the information about the depth position of the defects in the current state of development is lost. How this disadvantage can be rectified by means of signal theory is subject of current research. In addition to the suspected gas accumulations in the SAM images, various stamp marks can be seen in the anode-sheet photos in figure 5. At these locations, the separator was fixed to the anode by the cell manufacturer. These stamp marks are also visible in [22] and other unrecorded cell openings at our institute. Especially in 5B and C, increased silvery/greyish shimmering deposits are optically visible around the stamp marks. Based on the SAM images, we suspect that both the bulges and thus the alleged gas accumulations originated from these deposits. However, since all these spots are covered with gas accumulations in cell 2, they are not explicitly visible, since the gas reflects the signal almost completely and thus hardly anything arrives at the receiving sensor. In order to demonstrate different resolutions, a 500 µm/pixel resolution was chosen for the analysis of cell 3 as shown in figure 5C. In the analysis of cell 3, the focus still remains on the signal amplitude (first column in figure 5C) for now. Again, elliptical and non-elliptical spots are visible on the SAM image. However, as the cell case appeared much flatter and more individual spots are visible on the SAM image, there seems to have been less gassing in this cell compared to cell 2. The increased resolution of the SAM images leads to a slightly improved recognition of shapes. Large areas with an SA between 0.1 V and 0.05 V are now visible. Since this signal amplitude is not low enough to originate from a complete reflection, it can be assumed that these spots originate from the covering layers and/or inhomogeneous electrolyte distribution. This assumption is supported by the high correlation of shape and position of covering layers in the photo of the anode (see figure 5**C** third column).

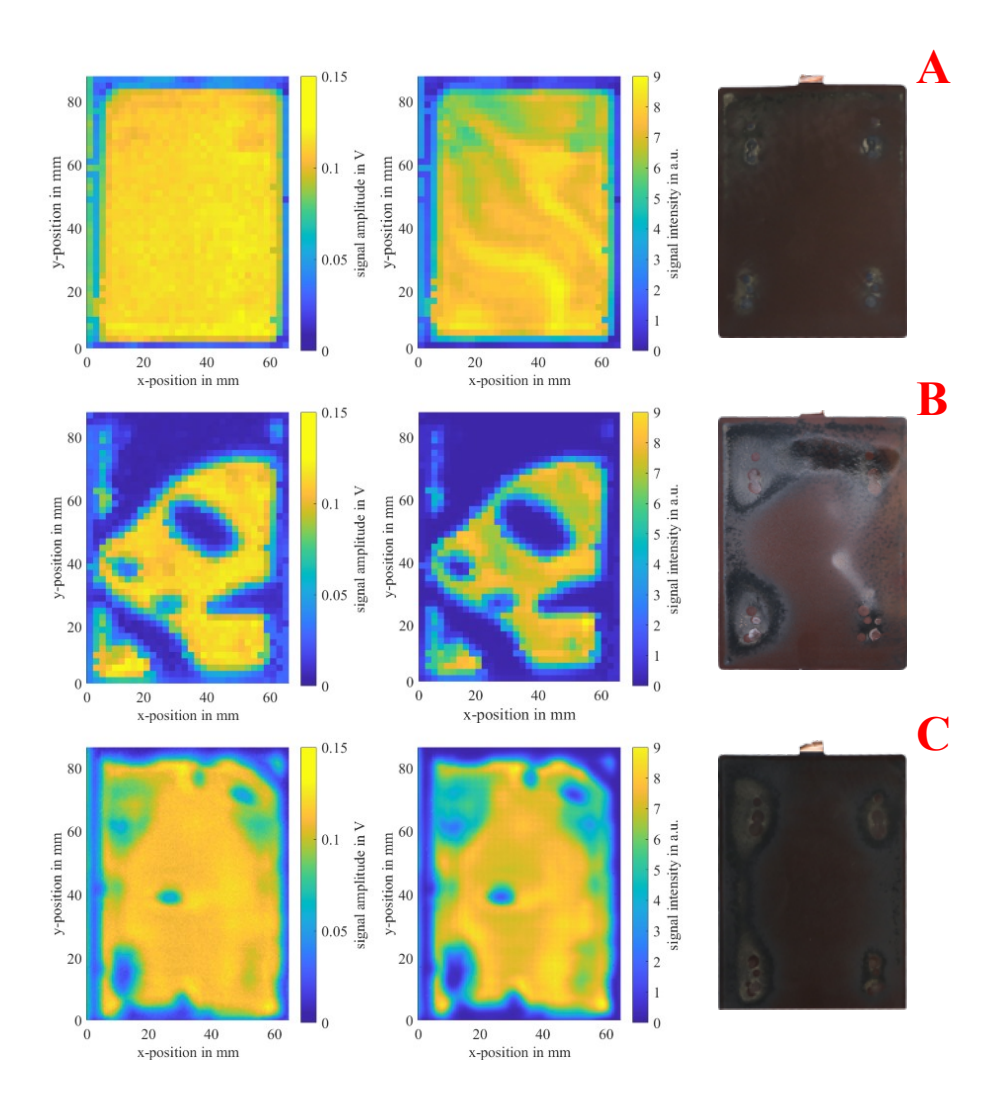


Figure 5: Comparison of the SAM images to an exemplary anode sheet. For each cell, the SA (first column) is compared with the SI (second column). In the third column, a representative back side of the anode sheets from the center of the cell-stack is displayed. To rectify this, the SAM images have been mirror-inverted so that they are congruent with the backs of the anode-sheets. **A** and **B** are showing cell 1 and cell 2 with a resolution of 2000  $\mu$ m/pixel. **C** is showing cell 3 with a resolution of 500  $\mu$ m/pixel resolution. Reading from top to bottom, cell 1 is displayed first, then cell 2 and finally cell 3.

In addition to these spots, elliptical spots with low signal amplitude are visible

in the centre of the cell. Again, as with cell 2, no deposits are visible at these locations on the anode sheets of the cell, indicating gas bubbles. Now the analysis of the most lightly strained cell 1 is carried out. Here, no significant bulges are visible on the surface of the cell. Furthermore, the signal amplitude is very homogeneous. To demonstrate the usefulness of the SI feature, the second column of figure 5A is now considered. Obviously, some structures are now visible here that were not visible in the SA-image. For one thing, the deposit and the stamp marks are now clearly visible in the upper left corner. Furthermore, bifurcated structures are visible emanating from the upper right corner, which were not at all visible from the SA alone. In the corresponding photo of the anode sheet, the strongest silvery/greyish deposits of the sheet are visible in the upper left corner (which appears on the upper right corner of the SI-SAM images because the sheets are turned around), so that it can be strongly assumed that these structures on the SI-SAM image are gas inclusions originating from these accumulations. Furthermore, several stream-like structures with particularly high signal intensity are visible following the suspected gas accumulations. According to [28], due to the increased signal intensity and the shape of the structures, it can be assumed that they are spots where an increased amount of electrolyte is present, as it has been displaced from the gas from the upper right corner. Due to the increased electrolyte occurrence, an improved mechanical propagation of the ultrasonic signal through the cell is possible at these locations, so that the SI is increased there. The same effect can be observed in the lower right corner of the second column in figure 3C for example, which also shows the SI. There, next to the spot with almost zero SI, is a semicircle-shaped area with nearly the maximum SI. However, since there is still a minimal basis for this in the ultrasound-related literature, it remains in the context of this work only a conjecture, which must be confirmed in the future with alternative imaging methods such as CT or in-situ neutron diffraction [29]. To make a quantitative statement about the electrochemical properties of the cell based on the ultrasound images, the state of research is not yet sufficiently developed. Detailed models with precisely determined material constants of all relevant occurring effects are required for this, both of which are still the subject of current research.

In conclusion, the SI feature provides a generally better image than SA, since more information of the ultrasound signal is used and reflections that are only noticeable in the later part of an ultrasound signal are also taken into account. To further understand which electrochemical effect led to the SAM images, a post-mortem analysis was performed. Whose results are presented now.

## 3.2. SEM Analysis

In this section, the results of the scanning electron microscopy (SEM) analysis are shown. Since the cell has to be disassembled to acquire SEM images of individual sheets, the gas bubbles mentioned previously will inevitably not be visible. All SEM images were taken with a ZEISS SUPRA 55 using the SE2 detector with a working distance of 4.0-6.0 mm and an acceleration voltage of 3 kV (except for the overview image (figure 8A), where 5 kV were used). The pouch cells were opened and prepared in an argon-filled glovebox and then transferred with a transfer module (Kammrath & Weiss GmbH) from the glovebox into the SEM. With the transfer shuttle the specimens are be protected from air and/or moisture at all times, so that no unwanted reaction with these during the transfer takes place. It should be mentioned again that the cells were stored for 9 months between the aging tests and SAM/SEM analysis. Although the long storage time allowed us to see both gas and covering layers with a high confidence at the same time, most of the internal processes associated with the cell-cycling should have subsided and the silver/grevish deposited material next to the stamp marks seen in e.g. figure 6B should be passivated.

Figure 6 shows an image of an anode sheet from cell 2. The sheet is from the middle of the electrode stack and the SEM results shown here as an example are comparable to the other available anode sheets. Due to the fact that no pristine cell material was available for the SEM analysis, two measurement areas were chosen (see figure 6B and C), a less silver/greyish spot in the middle of the sheet (C) and a spot directly at a stamp mark position (B).

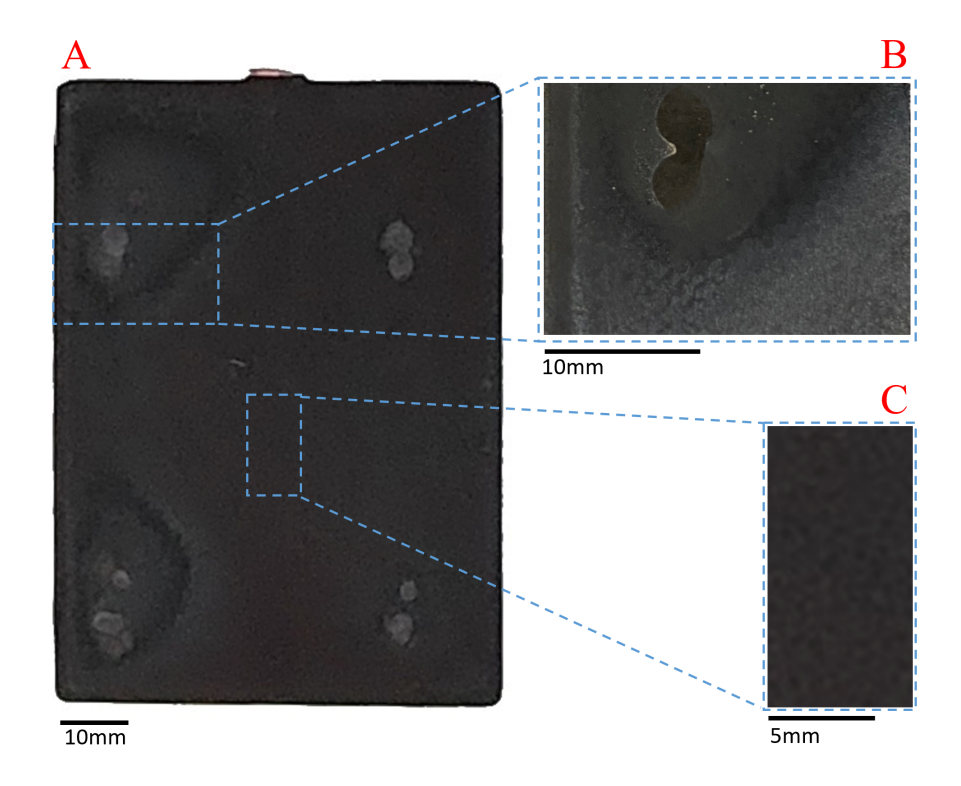


Figure 6: A Image of a node sheet from cell 2 with marked SEM measuring areas. B Zoom to stamp marks and  ${\bf C}$  reference area

In figure 7 the SEM results from the reference measurement at the center of the anode sheet are shown. In the reference image graphite flakes with slight contamination in the nano-size range are visible. In comparison to Liu et al. [30], the slight impurities could be lithium deposits, which might be explained by the fact that the cell was cycled under severe conditions, which favored the deposition (cell at 75.5% residual capacity; see table 1).

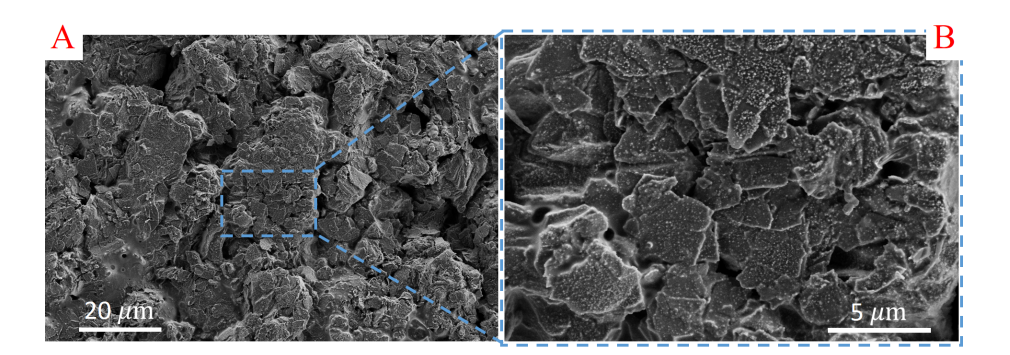


Figure 7: SEM images of the reference area in the center of the anode sheet (see figure  $6\mathbf{C}$ ). In  $\mathbf{B}$  (magnification of  $\mathbf{A}$ ), graphite flakes with slight impurities can be seen. It is assumed that the impurities are lithium deposits.

Figure 8A and B give an overview of the surface around the stamp marks. Two large circles with partially filled material are visible. The filled material (shown darker here) is the separator, which adheres to the anode even after the cell is disassembled. In figure 8C and D a close-up on the transition area between inside and outside the stamp mark is shown. Small remains of the separator are visible in the stamp mark area and in addition a large height difference in the transition area can be observed. In figure 8D graphite flakes are visible under the area where the separator was previously connected. This indicates that no, or at least significantly less new surface deposition material formed directly beneath the area where the separator was connected to the anode. In contrast, the areas directly adjacent to the stamp marks are completely covered with a thick surface layer. Additionally the covering layer has small holes going down to the graphite material (see figure 8E and F) and little surface damages (see figure 8G and H).

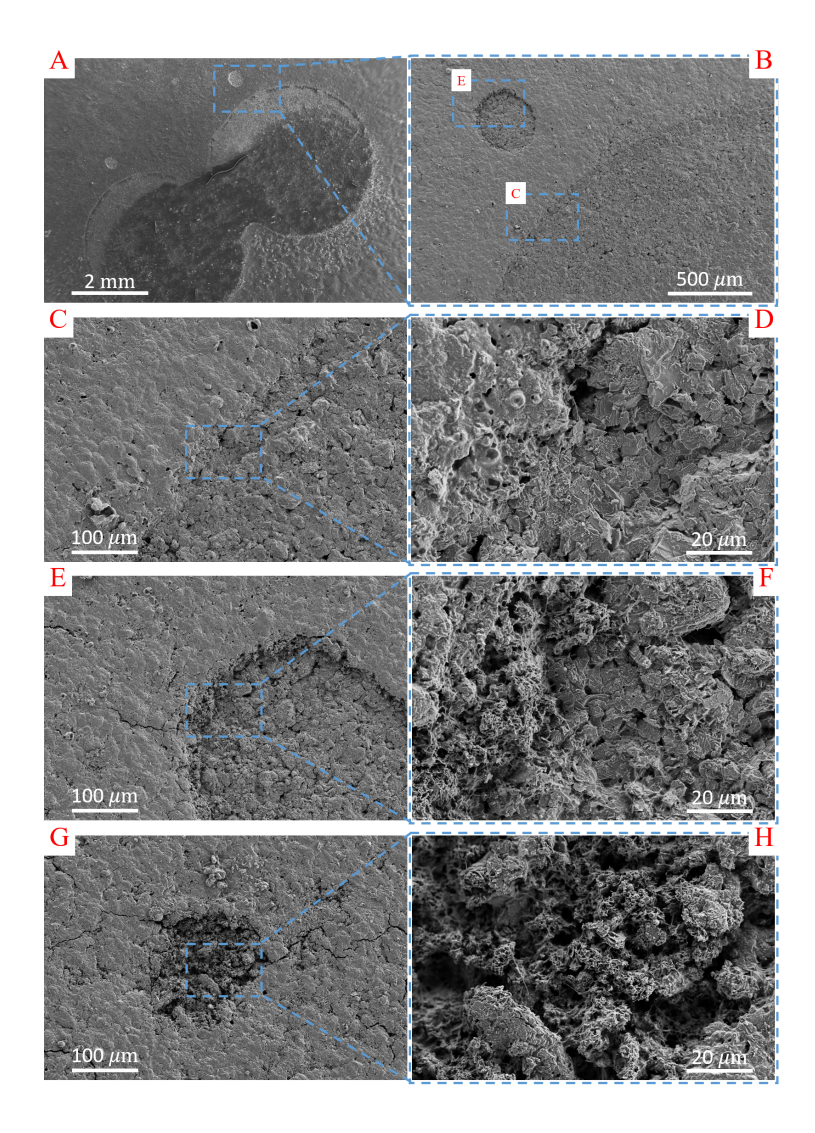


Figure 8: SEM images of the area around the stamp marks (see figure  $6\mathbf{B}$ ).  $\mathbf{A}$  and  $\mathbf{B}$  give an overview of the surface around the stamp marks.  $\mathbf{C}$  and  $\mathbf{D}$  show a close-up on the transition area between inside and outside the stamp marks.  $\mathbf{E}$  and  $\mathbf{G}$  with the magnified images  $\mathbf{F}$  and  $\mathbf{H}$  show the morphology of the covering layer in the presence of small surface holes and surface damage

So far, it is not clear where the small holes and/or surface damage came from, but it is assumed that they occurred during the disassembly (removal of the separator) or sample preparation of the SEM sample. At these spots, the morphology of the covering material can be seen. Compared to Louli et al. [31], the morphology looks like plated lithium. A possible explanation for this could be that in the area of the stamp marks the Li-ion transport is blocked (e.g. due to a lack of electrolyte, or clogged seperator at these locations) and therefore the local current density in the surrounding areas are increased which favors the accumulation of lithium plating [32, 33, 34]. The unwanted plated lithium can afterward react with the electrolyte forming a passivation layer and producing gas which can probably both be seen in the SAM images [35]. In a study by Cannarell and Arnold the effect of a locally clogged separator has been studied specifically investigated [36]. In this work, a cell with a locally clogged separator was purposefully built and cycled. After opening the cell, local lithium plating could be detected around the site of the clogging. A subsequent finite element simulation showed that an increased current density occurred around the edge of the clogged separator, leading to a local potential of < 0 V and thus to lithium plating. The overwhelming optical similarity of both separator and active material supports the assumption that exactly this effect also occurred in the production process of the cell in our work.

## 4. Conclusion

To image the aging of three NMC pouch cells with adjustable resolution, a low-cost SAM device was developed in this work. It was demonstrated that the clamping pressure is strongly related to the aging of the cells. In this work, increased covering layer formation on inhomogeneities produced by the cell manufacturer were observed at high clamping pressures. These covering layers (and resulting gas accumulations) have been imaged in advance with the developed SAM apparatus. Through SEM investigations it can be suspected that the covering layers are lithium plating. The cell which was clamped with the lowest pressure showed a much more homogeneous SAM image. Improved images were generated by applying the SI in lieu of it's SA feature in all SAM measurements. In particular, the slight inhomogeneities in the most lightly clamped cell also

became imageable. By using the through-transmission method, all cell layers could be imaged simultaneously without turning or moving the cell. Although the focus of ultrasound diagnosis has been on pouch cells, current research at our institute is aimed at extending these methods to alternative cell geometries such as prismatic or cylindrical cells. We hope that the publication of this low-cost SAM apparatus will contribute to the base of non-destructive imaging techniques and enable other research institutions and the industry to produce SAM images.

## 5. Acknowledgement

This work was funded by the Federal Ministry of Education and Research as part of the research cluster "Batterienutzungskonzepte" through the project MADAM4Life (grant number 03XP0327C) and as part of the research cluster "AQua" through the project InOPlaBat (grant number 03XP0352A). Furthermore, we have enjoyed conversations with Christiane Rahe, Alexander Blömeke and Philipp Dechent.

## References

- [1] Federal Ministry of Education and Research BMBF, Elektromobilität: Das auto neu denken. URL https://www.bmbf.de/de/elektromobilitaet-das-auto-neu-denken-567. html
- [2] N. Nitta, F. Wu, J. T. Lee, G. Yushin, Li-ion battery materials: present and future, Materials Today 18 (5) (2015) 252–264. doi:10.1016/j.mattod. 2014.10.040.
- [3] M. Ghiji, V. Novozhilov, K. Moinuddin, P. Joseph, I. Burch, B. Suendermann, G. Gamble, A review of lithium-ion battery fire suppression, Energies 13 (19) (2020) 5117. doi:10.3390/en13195117.

- [4] N. Williard, W. He, C. Hendricks, M. Pecht, Lessons learned from the 787 dreamliner issue on lithium-ion battery reliability, Energies 6 (9) (2013) 4682–4695. doi:10.3390/en6094682.
- [5] L. K. Willenberg, P. Dechent, G. Fuchs, D. U. Sauer, E. Figgemeier, Highprecision monitoring of volume change of commercial lithium-ion batteries by using strain gauges, Sustainability 12 (2) (2020) 557. doi:10.3390/ su12020557.
- [6] S. Hao, S. R. Daemi, T. M. Heenan, W. Du, C. Tan, M. Storm, C. Rau, D. J. Brett, P. R. Shearing, Tracking lithium penetration in solid electrolytes in 3d by in-situ synchrotron x-ray computed tomography, Nano Energy 82 (2021) 105744. doi:10.1016/j.nanoen.2021.105744.
- [7] S. Chandrashekar, N. M. Trease, H. J. Chang, L.-S. Du, C. P. Grey, A. Jerschow, 7li mri of li batteries reveals location of microstructural lithium, Nature materials 11 (4) (2012) 311–315. doi:10.1038/nmat3246.
- [8] N. Sharp, P. ORegan, D. Adams, J. Caruthers, A. David, M. Suchomel, Lithium-ion battery electrode inspection using pulse thermography, NDT & E International 64 (1) (2014) 41-51. doi:10.1016/j.ndteint.2014. 02.006.
- [9] A. G. Hsieh, S. Bhadra, B. J. Hertzberg, P. J. Gjeltema, A. Goy, J. W. Fleischer, D. A. Steingart, Electrochemical-acoustic time of flight: in operando correlation of physical dynamics with battery charge and health, Energy & Environmental Science 8 (5) (2015) 1569–1577. doi:10.1039/c5ee00111k.
- [10] A. Gitis, Flaw detection in the coating process of lithium-ion battery electrodes with acoustic guided waves, RWTH Aachen University, 2017. doi:10.18154/RWTH-2017-09951.
- [11] G. Davies, Characterization of batteries using ultrasound: Applications for battery management and structural determination, ProQuest Dissertations & Theses, Ann Arbor, 2018.

[12] R. Ruess, S. Schweidler, H. Hemmelmann, G. Conforto, A. Bielefeld, D. A. Weber, J. Sann, M. T. Elm, J. Janek, Influence of NCM particle cracking on kinetics of lithium-ion batteries with liquid or solid electrolyte, Journal of The Electrochemical Society 167 (10) (2020) 100532. doi:10.1149/1945-7111/ab9a2c.

URL https://doi.org/10.1149/1945-7111/ab9a2c

[13] K. Takahashi, V. Srinivasan, Examination of graphite particle cracking as a failure mode in lithium-ion batteries: A model-experimental study, Journal of The Electrochemical Society 162 (4) (2015) A635–A645. doi: 10.1149/2.0281504jes.

 ${
m URL} \ {
m https://doi.org/10.1149/2.0281504jes}$ 

- [14] A. Wuersig, W. Scheifele, P. Novak, CO[sub 2] gas evolution on cathode materials for lithium-ion batteries, Journal of The Electrochemical Society 154 (5) (2007) A449. doi:10.1149/1.2712138. URL https://doi.org/10.1149/1.2712138
- [15] A. Wang, S. Kadam, H. Li, S. Shi, Y. Qi, Review on modeling of the anode solid electrolyte interphase (sei) for lithium-ion batteries, npj Computational Materials 4 (1) (2018) 15. doi:10.1038/s41524-018-0064-0. URL https://doi.org/10.1038/s41524-018-0064-0
- [16] L. W. S. Jr., Fundamentals of Ultrasonic Nondestructive Evaluation A Modeling Approach, Springer, Berlin, Heidelberg, 2016.
- [17] G. Davies, K. W. Knehr, B. van Tassell, T. Hodson, S. Biswas, A. G. Hsieh, D. A. Steingart, State of charge and state of health estimation using electrochemical acoustic time of flight analysis, Journal of The Electrochemical Society 164 (12) (2017) A2746-A2755. doi:10.1149/2.1411712jes.
- [18] Y. Wu, Y. Wang, W. K. C. Yung, M. Pecht, Ultrasonic health monitoring of lithium-ion batteries, Electronics 8 (7) (2019) 751. doi:10.3390/ electronics8070751.

- [19] J. Sieg, M. Storch, J. Fath, A. Nuhic, J. Bandlow, B. Spier, D. U. Sauer, Local degradation and differential voltage analysis of aged lithium-ion pouch cells, Journal of Energy Storage 30 (2020) 101582. doi:https://doi.org/10.1016/j.est.2020.101582. URL https://www.sciencedirect.com/science/article/pii/S2352152X20305235
- [20] L. P. Bauermann, L. V. Mesquita, C. Bischoff, M. Drews, O. Fitz, A. Heuer, D. Biro, Scanning acoustic microscopy as a non-destructive imaging tool to localize defects inside battery cells, Journal of Power Sources Advances 6 (12) (2020) 100035. doi:10.1016/j.powera.2020.100035.
- [21] D. Wasylowski, Scanning acoustic imaging, https://git.rwth-aachen.de/isea/scanning-acoustic-imaging.
- [22] G. Fuchs, L. Willenberg, F. Ringbeck, D. U. Sauer, Post-mortem analysis of inhomogeneous induced pressure on commercial lithium-ion pouch cells and their effects, Sustainability 11 (23) (2019) 6738. doi:10.3390/su11236738.
- [23] J. Cannarella, C. B. Arnold, Stress evolution and capacity fade in constrained lithium-ion pouch cells, Journal of Power Sources 245 (2014) 745-751. doi:https://doi.org/10.1016/j.jpowsour.2013.06.165. URL https://www.sciencedirect.com/science/article/pii/ S037877531301197X
- [24] A. S. Mussa, M. Klett, G. Lindbergh, R. W. Lindström, Effects of external pressure on the performance and ageing of single-layer lithium-ion pouch cells, Journal of Power Sources 385 (2018) 18-26. doi:https://doi.org/10.1016/j.jpowsour.2018.03.020. URL https://www.sciencedirect.com/science/article/pii/ S0378775318302441
- [25] M. Lewerenz, A. Warnecke, D. U. Sauer, Introduction of capacity difference analysis (cda) for analyzing lateral lithium-ion flow to determine the state

- of covering layer evolution, Journal of Power Sources 354 (2017) 157–166. doi:https://doi.org/10.1016/j.jpowsour.2017.04.043.
- [26] L. Aguiar-Conraria, M. J. Soares, The continuous wavelet transform: Moving beyond uni- and bivariate analysis, Journal of Economic Surveys 28 (2) (2014) 344-375. arXiv:https://onlinelibrary.wiley.com/doi/pdf/10.1111/joes.12012, doi:https://doi.org/10.1111/joes.12012. URL https://onlinelibrary.wiley.com/doi/abs/10.1111/joes. 12012
- [27] G. Georgiou, F. Cohen, Tissue characterization using the continuous wavelet transform. i. decomposition method, IEEE Transactions on Ultrasonics, Ferroelectrics, and Frequency Control 48 (2) (2001) 355–363. doi:10.1109/58.911718.
- [28] Z. Deng, Z. Huang, Y. Shen, Y. Huang, H. Ding, A. Luscombe, M. Johnson, J. E. Harlow, R. Gauthier, J. R. Dahn, Ultrasonic scanning to observe wetting and "unwetting" in li-ion pouch cells, Joule 4 (9) (2020) 2017– 2029. doi:https://doi.org/10.1016/j.joule.2020.07.014.
- [29] D. Beck, P. Dechent, M. Junker, D. U. Sauer, M. Dubarry, Inhomogeneities and cell-to-cell variations in lithium-ion batteries, a review, Energies 14 (11) (2021). doi:10.3390/en14113276.
  URL https://www.mdpi.com/1996-1073/14/11/3276
- [30] H. Liu, X. Cheng, R. Zhang, P. Shi, X. Shen, X. Chen, T. Li, J. Huang, Q. Zhang, Mesoporous graphene hosts for dendrite-free lithium metal anode in working rechargeable batteries, Transactions of Tianjin University 26 (2) (2020) 127–134. doi:https://doi.org/10.1007/s12209-020-00241-z.
- [31] A. J. Louli, M. Genovese, R. Weber, S. Hames, E. Logan, J. Dahn, Exploring the impact of mechanical pressure on the performance of anode-free lithium metal cells, Journal of The Electrochemical Society 166 (8) (2019) A1291. doi:http://dx.doi.org/10.1149/2.0091908jes.

- [32] F. Ringbeck, C. Rahe, G. Fuchs, D. U. Sauer, Identification of lithium plating in lithium-ion batteries by electrical and optical methods, Journal of The Electrochemical Society 167 (9) (2020) 090536. doi:https://doi.org/10.1149/1945-7111/ab8f5a.
- [33] C. Uhlmann, J. Illig, M. Ender, R. Schuster, E. Ivers-Tiffée, In situ detection of lithium metal plating on graphite in experimental cells, Journal of Power Sources 279 (2015) 428–438. doi:http://dx.doi.org/10.1016/j.jpowsour.2015.01.046.
- [34] T. Waldmann, B.-I. Hogg, M. Wohlfahrt-Mehrens, Li plating as unwanted side reaction in commercial li-ion cells—a review, Journal of Power Sources 384 (2018) 107–124. doi:https://doi.org/10.1016/j.jpowsour.2018. 02.063.
- [35] Q. Liu, D. Xiong, R. Petibon, C. Du, J. Dahn, Gas evolution during unwanted lithium plating in li-ion cells with ec-based or ec-free electrolytes, Journal of the Electrochemical Society 163 (14) (2016) A3010. doi:http://dx.doi.org/10.1149/2.0711614jes.
- [36] J. Cannarella, C. Arnold, The effects of defects on localized plating in lithium-ion batteries, Journal of the Electrochemical Society 162 (2015) A1365-A1373. doi:10.1149/2.1051507jes.